

Added value of solar radiation in snowmelt models: benchmarking empirical models in the High Atlas Range, Morocco

HAFSA BOUAMRI¹, Christophe Kinnard², Abdelghani BOUDHAR¹, Simon Gascoin³, Lahoucine Hanich^{4,5}, and Abdelghani CHEHBOUNI⁶

¹Sultan Moulay Slimane University Faculty of Science and Technology

²Université du Québec à Trois-Rivières

³Centre d'Études Spatiales de la Biosphère (CESBIO), University of Toulouse, CNRS/CNES/IRD/UPS

⁴Cadi Ayyad University

⁵Faculty of Sciences & Techniques, Cadi Ayyad University

⁶Mohammed VI Polytechnic University

July 13, 2020

Abstract

Estimating snow water equivalent (SWE) and snowmelt in semi-arid mountain ranges is an important but challenging task, due to the large spatial variability of the seasonal snow cover and scarcity of field observations. Adding solar radiation as snowmelt predictor within empirical snow models is often done to account for topographically induced variations in melt rates, at the cost of increasing model complexity. This study examines the added value of including different treatments of solar radiation within empirical snowmelt equations. Three spatially-distributed, enhanced temperature index models that respectively include the potential clear-sky direct radiation (HTI), the incoming solar radiation (ETIA) and net solar radiation (ETIB) were compared with a classical temperature-index model (TI) to simulate SWE within the Rheraya basin in the Moroccan High Atlas Range. Extensive model validation of simulated snow cover area (SCA) was carried out using blended MODIS snow cover products over the 2003-2016 period. We found that models enhanced with a radiation term, particularly ETIB which includes net solar radiation, better explain the observed SCA variability compared to the TI model. However, differences in model performance were overall small, as were the differences in basin averaged simulated SWE and melt rates. SCA variability was found to be dominated by elevation, which is well captured by the TI model, while the ETIB model was found to best explain additional SCA variability. The small differences in model performance for predicting spatiotemporal SCA variations is interpreted to results from the averaging out of topographically-induced variations in melt rates simulated by the enhanced models, a situation favored by the rather uniform distribution of slope aspects in the basin. Moreover, the aggregation of simulated SCA from the 100 m model resolution towards the MODIS resolution (500 m) suppresses key spatial variability related to solar radiation, which attenuates the differences between the TI and the radiative models.

Introduction

Snow constitutes a key element in determining water availability in mountainous catchments, especially in arid and semiarid regions, so that a good understanding of snowpack processes is crucial to support water management strategies (Barnett, Adam, & Lettenmaier, 2005; De Jong, Lawler, & Essery, 2009; Vicuña, Garreaud, & McPhee, 2011; Viviroli & Weingartner, 2008). Snowmelt and snow water equivalent assessment using modelling techniques at the basin scale is therefore an important tool for water budget calculation and

runoff prediction (Bair, Rittger, Davis, Painter, & Dozier, 2016; Fayad et al., 2017; Han et al., 2019; Matin & Bourque, 2013).

The Atlas mountain range in Morocco plays an important role in socio-economic development by providing fresh water to irrigate the arid plains downstream and provide drinking water for populations and hydropower generation (Chehbouni et al., 2008). In the headwater basins of these chains, streamflow is largely generated from meltwater supplied by the snowpack during spring and early summer (Boudhar et al., 2009; Boudhar et al., 2020; Hajhouji et al., 2018; Schulz & de Jong, 2004). With the current situation of water resources scarcity induced by increasing demand due to both population growth and economic development, snowpack monitoring and modelling appears as an essential task to support policy-making and decisions for water resources management.

The lack of ground observations, but also the high temporal and spatial heterogeneity of snow cover driven by highly variable temperatures, orographic precipitation and complex topography, represent challenging limitations for snow studies in the Atlas range (Boudhar, Boulet, Hanich, Sicart, & Chehbouni, 2016; Boudhar et al., 2010; Chaponnière et al., 2005; Marchane et al., 2015). In this context, the use of simple conceptual snow models combined with remote sensing data constitutes a useful approach to assess and quantify snowmelt and SWE distribution at the basin scale. Conceptual models use simplified process representations with lower data requirements than physically based models, and are thus widely used for large-scale applications in high mountain catchments where in situ observations are sparse (Fassnacht et al., 2017; Schneider, Kilian, & Glaser, 2007; Singh & Bengtsson, 2003). The most commonly used conceptual snow models are temperature-index models, which depend solely on air temperature to calculate snowmelt (Hock, 2003). Despite their simplicity, these models can provide reliable estimates of melt rates and perform generally well both at the point scale and within distributed or lumped hydrological models (Abudu, Cui, Saydi, & King, 2012; Hublart et al., 2016; Kampf & Richer, 2014; Réveillet, Vincent, Six, & Rabatel, 2017; Senzeba, Bhadra, & Bandyopadhyay, 2015; Vincent, 2002). On the other hand, it has been demonstrated that enhanced temperature-index models including solar radiation can outperform classical degree-day models (Bouamri, Boudhar, Gascoin, & Kinnard, 2018; Carenzo, Pellicciotti, Rimkus, & Burlando, 2009; Gabbi, Carenzo, Pellicciotti, Bauder, & Funk, 2014; Hock, 1999; Homan, Luce, McNamara, & Glenn, 2011; Pellicciotti et al., 2005).

Solar radiation is one of the main components of the surface energy balance, generally contributing between 50 and 90% of the energy available for melt (Mazurkiewicz, Callery, & McDonnell, 2008; Willis, Arnold, & Brock, 2002), and has a great influence on the spatial variability of ablation (Aguilar, Herrero, & Polo, 2010; Boudhar et al., 2016; Comola et al., 2015; Herrero, Polo, Moñino, & Losada, 2009). However, representing the spatial variability within distributed snowmelt models for hydrological applications remains challenging, especially in mountainous areas where the snow distribution depends on complex relationships between meteorological conditions and the surrounding landscape, primarily topography (Allen, Trezza, & Tasumi, 2006; Anderton, White, & Alvera, 2004; Grünewald, Schirmer, Mott, & Lehning, 2010; Molotch, Colee, Bales, & Dozier, 2005).

In this sense, various studies showed that altitude, slope, and aspect play a crucial role in determining the spatial variability of snow process (Lehning et al., 2006; Letsinger & Olyphant, 2007; López-Moreno & Stähli, 2008). Interactions between topography and solar radiation strongly modulates the shortwave radiation balance and produce considerable shading effect, especially in high relief landscapes (e.g. Olyphant, 1984). In the semiarid, subtropical context of the Atlas Range, solar radiation is expected to be significant for spatial SWE modeling (López-Moreno et al., 2017) considering that (i) solar radiation strikes the Earth surface at a large elevation angle during spring over subtropical regions, delivering more heat per unit area; (ii) the arid climate favors the transmissivity of solar radiation and the sparse vegetation favors high absorption of solar irradiance by the surface; (iii) the pronounced topographic variability should cause heterogeneous radiation loading on slopes (Baba, Gascoin, Kinnard, Marchane, & Hanich, 2019).

A previous study by Bouamri et al. (2018) demonstrated that snow ablation models enhanced with solar radiation outperformed the simple temperature index (TI) (e.g. Hock, 2003) model at the point (station) scale

and were also more transferable between years, when model parameters were calibrated over a single year. However, model performances were more similar when models were calibrated on a longer (4 year) period. In this present study, we aim to further assess the contribution of solar radiation to the spatiotemporal variability of simulated snowmelt and SWE at the basin scale in the Atlas range. Given the significant computational cost entailed to calculate spatially distributed radiation fields, it is important to assess their relevance for estimating snowmelt with conceptual models aimed for hydrological applications. Hence, a particular focus of this study is to benchmark the performance of enhanced models including different treatments of solar radiation, relative to the reference temperature index model.

Study area

The present work was carried out in the Rheraya watershed located in the High Atlas range in central Morocco (Figure 1). The Rheraya watershed has a mixed snow-rain regime and constitutes the most important water supply for the downstream region (Chaponnière et al., 2005; Hajhouji et al., 2018; Rochdane, Reichert, Messouli, Babqiqi, & Khebiza, 2012; Schulz & de Jong, 2004). The snow cover is highly variable at annual and inter-annual time scales and the snowmelt was found to contribute from 28 to 48% of the annual river discharge (Boudhar et al., 2009). Average annual precipitation was 520 mm from 1988 to 2010 as measured at the Club Alpin Francais (CAF) station at 2650 m above sea level (a.s.l), where 50% occurred as snow during winter months (Boudhar et al., 2016). This basin covers an area of 228 km², ranging in altitude from 1060 m a.s.l to a culminating point on the Jbel Toubkal summit, the highest summit of North Africa at 4167 m a.s.l. In terms of topography, the slopes are steep (mean of ~24% from a 100 m resolution DEM) and characterized by sparse vegetation in the spring which quickly disappear due to aridity. The Rheraya has been used as an experimental site for mountain hydrological studies in the Tensift River basin (Jarlan et al., 2015), leading to a concentration of studies on snow and hydrology in this basin (Baba, Gascoin, Jarlan, Simonneaux, & Hanich, 2018; Baba et al., 2019; Bouamri et al., 2018; Boudhar et al., 2016; Hajhouji et al., 2018).

Data and methods

Digital Elevation Model

A 4 m spatial resolution Digital Elevation Model (DEM) derived from Pleiades stereoscopic imagery was used to represent the basin topography. Details about DEM processing are provided in Baba et al. (2019). The DEM was previously validated for the Rheraya catchment, showing a vertical absolute accuracy of 4.72 m (Baba et al., 2019). The DEM was aggregated to a coarser 100 m resolution using bilinear resampling. This resolution was chosen as a good tradeoff allowing for a reasonable model computation time while adequate representing the dominant topographic features in the Rheraya catchment (Baba et al., 2019).

Meteorological forcing data

Available meteorological observations were obtained from ten stations at various locations within the Rheraya watershed (Table 1, Figure 1). We used daily meteorological data retrieved from these weather stations, nine located within the Rheraya watershed and one station outside the catchment boundaries. The type of variable measured and period of available observations varied between the stations over the studied period (2003-2016). While precipitation measurements were available at all ten stations, the availability of air temperature and relative humidity varied among stations and over time (Figure 2). Oukaimeden-SM (3230 m a.s.l.) is the only station with significant snowfall measuring all meteorological variables including total precipitation. However, historical precipitation was measured with an unheated tipping-bucket rain-gauge, which yields unreliable snowfall in winter (Bouamri et al., 2018). The lower altitude CAF station (2612 m a.s.l.) has more

reliable precipitation observations, since rainfall and snowfall are independently and manually measured since 1988 (Figure 1). Despite its location outside, but near the catchment boundary, the CAF station is crucial in this study to distribute precipitation at high elevations. Because the high elevation stations Oukaimeden-SM and Neltner have unheated rain gauges, their precipitation records were excluded in order to avoid interpolating unreliable observations.

Satellite data

MODIS daily snow product

Snow cover maps in this study were derived from the Moderate Resolution Imaging Spectroradiometer (MODIS) daily snow cover products MOD10A1 and MYD10A1 (MODIS Snow Cover Daily L3 Global 500 m SIN GRID V006), respectively generated from the Terra and Aqua MODIS satellites, and acquired from the National Snow and Ice Data Center (NSIDC) (Hall & Riggs, 2016). The MODIS snow products from the Terra and Aqua satellites are available since February 2000 and February 2002, respectively. The datasets are produced in a Geographic projection and were re-projected to the World Geodetic System 1984 (WGS84) Universal Transverse Mercator (UTM) coordinate system using the data transformation options available at NSIDC. A total of 5818 MOD10A1 images and 5309 MYD10A1 images covering 13 years from September 2003 to August 2016, were used in this study.

Snow cover was identified using the Normalized Difference Snow Index (NDSI) (Hall, Riggs, & Salomonson, 1995), which captures the high contrast between the characteristically high reflectance of snow in the visible spectrum and its low reflectance in the shortwave infrared spectrum. Starting in MODIS version 6, the fractional snow cover (FSC) has been replaced by the NDSI which is designed to detect snow cover with high accuracy over a wide range of viewing conditions, besides providing more flexible data to the user (Riggs, Hall, & Román, 2016).

Processing and combining MOD10A1 and MYD10A1

Cloud obscuration is the main obstacle to using MODIS snow cover products (Parajka & Blöschl, 2008; Xie, Wang, & Liang, 2009; Zhou, Aizen, & Aizen, 2013). The Terra and Aqua satellites have an approximate 3 hours average overpass time difference, during which cloud conditions can change significantly (Xue, Wang, Xiao, Chen, & Liu, 2014). Various previous studies have shown that combining Terra and Aqua observations reduces cloud obscuration (Gafurov & Bárdossy, 2009; Gascoin et al., 2015; Parajka & Blöschl, 2008; Wang & Xie, 2009; Xie et al., 2009). For example, Gao, Xie, Yao, and Xue (2010) reported that combining Terra and Aqua improved cloud filtering, by reducing the influence of transient clouds in daily reflectance data by 11.7% compared to using MOD10A1 alone, and 7.7% compared to using MYD10A1 alone. In this study, the MOD10A1 and MYD10A1 were merged into a combined product called CMXD10A (Figure 3) as follow: (i) on any given day if only one source (either Terra or Aqua) was available it was used for that day; (ii) for days when both products are available, priority was given to the Terra product (e.g. Xie et al., 2009) since the Aqua MODIS instrument provides less accurate snow maps due to dysfunction of band 6 on Aqua (Gascoin et al., 2015; Riggs & Hall, 2004; Salomonson & Appel, 2006; Zhang et al., 2019). This means than any pixel classified as either cloud, missing, or unclassified in MOD10A1 was filled with the corresponding pixel in MYD10A1 if that pixel had a NDSI value, else the original MOD10A1 pixel classification was conserved (Figure 3).

Subsequently, a spatiotemporal filter was applied to the merged CMXD10A product to fill in missing NDSI data, i.e. pixels classified as cloud, but also those classified as either missing, saturated or unclassified, collectively referred to as ‘missing’ therein. A spatial filter was first applied only if less than 60% of the mountainous areas (elevations above 1000 m) were missing (Marchane et al., 2015). This filter classifies missing pixels as snow-covered when their elevations is higher than the average elevation of the snowy pixel for the entire basin. Then, a temporal filter was applied to linearly interpolate the remaining missing pixels within a moving window extending 3 days prior and 2 days after the current date. NDSI values in the blended

and interpolated CMXD10A product were converted to binary maps of snow cover area (SCA) based on an NDSI threshold of 0.4, following previous studies (Hall & Riggs, 2016; Marchane et al., 2015; Xiao, Zhang, Boles, Rawlins, & Moore, 2004), i.e., for each pixel, $SCA = 1$ when $NDSI \geq 0.4$, otherwise $SCA = 0$ (Figure 3). The blending and filtering procedure reduced the fraction of missing pixels to 0.84%, similar to previous results obtained in the same area by Marchane et al. (2015).

Snow models

Four different melt models were used to simulate SWE in the Rheraya watershed, ranging from a classical degree-day or ‘temperature index’ (TI) model (Hock, 2003), which uses air temperature as the sole predictor for melt, to ‘enhanced’ degree-day models that include solar radiation terms: (i) Hock’s temperature index melt model (HTI) including clear sky solar radiation (Hock, 1999); (ii) an enhanced temperature-index (ETIA) including global radiation (Pellicciotti et al., 2005) and (iii) an enhanced temperature-index (ETIB) that includes albedo (Pellicciotti et al., 2005) (Table 2). These models were previously calibrated and validated at the point scale at the Oukaimeden-SM weather station site (Bouamri et al., 2018), and the same model coefficients were used for the spatial simulations in this study (Table 3). Further model descriptions and results regarding model performances at the point scale are presented in detail in Bouamri et al. (2018), and only the main model equations are given in Table 2.

Sublimation losses are not accounted for in empirical melt models. These can be significant in the Rheraya basin, representing 7-20 % of annual snowfall (Boudhar et al., 2016). To take into account sublimation losses, a constant average mean daily sublimation rates was used over the entire basin (Table 3), based on the energy balance study at the Oukaimeden-SM site by Boudhar et al. (2016). While this approach is admittedly simple, it allows correcting for first order sublimation losses and as such avoid compensating these losses by reduced precipitation during interpolation, as can be the case when sublimation losses are completely ignored.

Spatialization of meteorological forcing

Half-hourly meteorological observations retrieved from the different weather stations were averaged to daily interval for the entire study period (2003-2016). Relative humidity (RH) observations was converted to dew point temperature (DP) following Liston and Elder (2006b), since RH is considered a non linear function of elevation; then mean monthly lapse rates for air temperature (T_a) and dew point temperature (DP) were determined by linear regression of these variables against elevation.

To distribute T_a and DP observations, station observations were first adjusted to a common elevation using the calculated lapse rate for each variable, and then spatially interpolated to the entire basin using the Barnes objective analysis scheme, following Liston and Elder (2006b). The Barnes scheme is used for interpolating data from irregularly spaced observations to a regular grid using a two-pass scheme (Barnes, 1964). It uses a Gaussian distance weighting function to interpolate observations to the regular grid, in which the weight that a station contributes to the grid point decreases with increasing distance from the point. The Barnes method was chosen after a comparative analysis of interpolation methods (nearest neighbor, Inverse Distance Weighting) in Rheraya, and showed that it results in smoother gridded fields and reduced errors compared to other methods. The interpolated values are then lapsed back to their original grid elevation using the same lapse rate, and the DP reconverted to RH.

Precipitation was spatially distributed by combining spatial interpolation with a non-linear lapse rate, following Liston and Elder (2006b). First, precipitation observations are interpolated to the model grid using the Barnes objective analysis scheme. A reference topographic surface is constructed by interpolating the station true elevations (as measured by GPS) using the same method. The modelled precipitation rate P_x (mm d⁻¹), at a grid point x with elevation Z_x is computed as:

$$P_x = P_0 \times \frac{[1+X(Z_x-Z_0)]}{[1-X(Z_x-Z_0)]} \quad (1)$$

Where P_0 is the interpolated station precipitation, Z_0 is the interpolated station elevation, and X (mm km^{-1}) is the precipitation lapse rate, or ‘correction factor’ (Liston & Elder, 2006b). This enhancement factor \mathcal{X} is referred to as the ‘precipitation lapse rate’ (PLR) hereafter. An interpolated topographic reference surface (Z_x) is used rather than a fixed reference because the precipitation adjustment function (equation (1)) is a nonlinear function of elevation (Liston & Elder, 2006b).

Due to the large spatial and temporal heterogeneity of observed precipitation in Rheraya, a specific calibration of PLR was sought. A range of 0.21- 0.35 km^{-1} was used based on an value optimized on weather station observations and the value suggested by Liston and Elder (2006b). The calibration-validation procedure was performed on the positives SWE changes, mostly reflecting snow accumulation, simulated by the distributed model at the AWS Oukaimeden-SM. PLR was calibrated over a lumped 3-year period (2003-2006) and validated separately on the remaining two years (2007-2008, 2009-2010).

The extrapolation of precipitation using equation (1) can result in unrealistically large accumulation rates at high elevations where there are few stations to constrain precipitation. Several studies have shown (Alpert, 1986; Collados-Lara, Pardo-Iguzquiza, Pulido-Velazquez, & Jimenez-Sanchez, 2018; Eeckman et al., 2017; Roe & Baker, 2006) that while precipitation typically increases with elevation in mountain basins due to orographic uplifting of air masses, this increase can cease and precipitation even decrease passed a certain elevation. This is caused by the progressive depletion of moisture available for condensation within the rising air mass. As such, it is crucial in hydrological modeling to limit the vertical extrapolation of precipitation to avoid artificial snow build up at high elevations. In this sense, Liston and Elder (2006b) limited the difference between the actual (Z_x) and interpolated (Z_0) station elevation ($Z = Z_x - Z_0$) to a default maximum value (Z_{max}) of 1800 m. In this study, this parameter was subjected to a calibration/validation procedure against the MODIS SCA maps for all melt models. Z_{max} was calibrated on odd years within a 300-1800 m range and validated on even years for each model in order to reduce the climate dependency of the calibration period (Arsenault, Brissette, & Martel, 2018). The validation was done using the optimal parameter for each model as well as with the mean of the optimal parameters of each model (mean Z_{max}).

The potential, clear-sky direct solar radiation was calculated as a function of solar geometry, topography and a constant vertical atmospheric transmissivity following Hock (1999), and includes topographic shading (Equation 4b in Table 2). Global radiation is calculated using a cloud factor parameterization based on relative humidity (Equation 5b, c in Table 2), and the net radiation uses an albedo parameterisation based on accumulated positive degree days (Equation 6b in Table 2). Further details are given in Bouamri et al. (2018).

Rain/snow partition

Determination of the precipitation phase remains decisive in hydrological modeling, especially in mountain areas, to distinguish between liquid and solid inputs (Marks, Winstral, Reba, Pomeroy, & Kumar, 2013; Yasutomi, Hamada, & Yatagai, 2011). Various approaches based on air temperature variable have been used, such as a single air temperature threshold (e.g. Fassnacht, Venable, Khishigbayar, & Cherry, 2013) or a varying snowfall fraction between two air temperature thresholds (e.g. Feiccabrino, Graff, Lundberg, Sandstrom, & Gustafsson, 2015; Marks et al., 2013). This linear transition technique was used for the rain-snow partition. The snowfall fraction is linearly interpolated between a temperature threshold for rain T_{rain} (degC), and a temperature threshold for snow T_{snow} (degC) (McCabe & Wolock, 1999; Moore, Trubilowicz, & Buttle, 2012; Tarboton & Luce, 1996). The daily snowfall (SF) and rainfall (RF) are computed as:

$$\text{SF} = P_x (T_{\text{rain}} - T_x) / (T_{\text{rain}} - T_{\text{snow}}) \quad (2a)$$

$$\text{RF} = P_x - \text{SF} \quad (2b)$$

Where P_x is total precipitation and T_x is air temperature at gridpoint x . If the daily air temperature is above the T_{rain} threshold then $\text{RF} = P_x$ and $\text{SF} = 0$, while if $T_x < T_{\text{snow}}$ then $\text{RF} = 0$ and $\text{SF} = P_x$. The two fixed temperature threshold, T_{rain} and T_{snow} , were calibrated on odd years and validated on even years using the total precipitation at the CAF station over 2003-2016 where manual observations of snowfall and rainfall are available. A range of -3 to 3°C was selected for calibration based on observed temperatures during recorded precipitations at the CAF station.

Model validation

The daily snow cover area (SCA) from the merged CMXD10A product was used to assess the ability of each model to simulate the spatiotemporal variability of snow cover in the Rheraya basin over the 2013-2016 period. A conversion of the simulated SWE to SCA was required in order to compare the simulated SCA with MODIS SCA. This conversion was performed using a constant threshold (SWE_0), i.e. for each grid, $\text{SCA} = 1$ when $\text{SWE} \geq \text{SWE}_0$ and $\text{SCA} = 0$ otherwise. The conversion was done at the model resolution (100 m). The use of this fixed threshold avoids more complex snow depletion curves that require more parameters unknown in our area (Magand, Ducharne, Le Moine, & Gascoin, 2014; Pimentel, Herrero, & Polo, 2017). Therefore, SWE_0 was subjected to the same calibration/validation procedure as for Z_{max} , using a range of values from 1 to 20 mm following previous studies (Baba et al., 2019; Gascoin et al., 2015)

Confusion matrices were used to assess the classification accuracy of the simulated SCA maps relative to MODIS SCA. Confusion matrices are two-dimensional contingency tables that display the discrete joint distribution of simulated and observed data frequencies (Zappa, 2008). Model skill scores were derived from the confusion matrix (Table 5). The Heidke Skill Score (HSS) (Heidke, 1926) which is equivalent to the Kappa coefficient proposed by Cohen (1960), measure the classification accuracy relative to that expected by chance and has been extensively used for imbalanced datasets, including snow remote-sensing studies (e.g. Baba et al., 2019; Notarnicola et al., 2013; Zappa, 2008). The HSS was thus the preferred global metrics used for model assessment. Still, because no global metric is able to completely depict the types of classification errors committed by a model, four metrics based on marginal ratios of the confusion matrix were also used to investigate model errors, as done in several previous studies (e.g. Parajka & Blöschl, 2012; Rittger, Painter, & Dozier, 2013; Zhang et al., 2019; Zhou et al., 2013). The true positive rate (TPR) measures the proportion of MODIS snow-covered pixels correctly identified as such by the model. Oppositely, the true negative rate (TNR) measures the proportion of MODIS snow-free pixels correctly simulated by the model. The false-negative rate (FNR) measures the proportion of MODIS snow-covered pixels incorrectly identified as snow-free by the model. Complementarily, the false-positive rate (FPR) or ‘False Alarm Rate’ (FAR) as called by Zappa (2008) is the proportion of MODIS snow-free pixels incorrectly identified as snow-covered by the model. Further descriptions of these metrics are given in Table 5.

Results

Point scale model calibration and validation

Rain/snow partition

The optimal values of T_{snow} and T_{rain} thresholds (Equation (2)) found from calibration were -2.5°C and 2.5°C respectively. Overall, the agreement between simulated and measured precipitation is fair with a moderate performance for rainfall ($\text{NSE} = 0.54$; $r = 0.75$), and higher performance for snowfall ($\text{NSE} = 0.77$, $r = 0.88$) (Figure 4a). The frequency analysis of precipitation events at the CAF station shows that snowfall-only events occurred at air temperatures up to $+5^\circ\text{C}$, while rainfall-only events can occur at temperature down to -5°C , with mixed events occurring within this -5°C to $+5^\circ\text{C}$ range (Figure 4b). The -2.5°C to $+2.5^\circ\text{C}$ calibrated range thus stands out as the best compromise to predict most

accurately absolute rain and snowfall quantities within this sensitive -5degC to +5degC interval. The better performance for snowfall is encouraging for the ensuing SWE modelling.

Calibration of PLR

The optimal value for the precipitation lapse rate (PLR) found from calibration against SWE measurements at the Oukaimeden-SM station was 0.35 km^{-1} . The performance among models is relatively similar during the lumped three-year calibration period (2003-2006) (Figure 5). The TI and HTI models show slightly better performances (NSE = 0.85) than the models including radiation (ETIA, NSE = 0.78) and albedo (ETIB, NSE = 0.83). All models present the worst prediction performances during calibration year 2003-2004, during which all models exaggerated ablation from mid December to mid February, especially for the ETIB model, while this model performed better than others in late spring (Figure 5a). Independent validation shows different results. In 2006-2007 the models performed unequally, particularly during the ablation period, with models that include radiation (ETIA) and albedo (ETIB) showing an overall better performance (NSE values of 0.60 and 0.78, respectively) than TI (NSE = -0.10) and HTI (NSE = 0.19) (Figure 5, Table 5). In 2009-2010 all models underestimated accumulation, with slight differences in ablation, and the TI model performed slightly better than other models (NSE = 0.58).

Overall, these results show that the simpler TI and HTI models performed slightly better in calibration than additive ETI models, but they transfer less well to independent validation years. This agrees with previous findings by Bouamri et al. (2018) who showed that enhanced ETI models transfer better to other years when calibrated on a short time period. However Bouamri et al (2018) used the observed accumulation rate to calibrate and validate the different melt models, in order to remove the influence of precipitation uncertainties on the calibration of the melt model coefficients (Table 3). The comparatively worst performance observed at the Oukaimeden-SM station in this study can thus be attributed to uncertainties in precipitation observations, rain-snow partition, and the spatial interpolation of precipitation, and highlights the notorious difficulties in distributing precipitations observations in mountainous basins (Gottardi, Obled, Gailhard, & Paquet, 2012).

Catchment-wide snow cover area

Parameter sensitivity and variability

The sensitivity of SCA model performance to the maximum elevation difference (Z_{\max}) and SWE-SCA conversion threshold (SWE_0) was assessed using the mean daily HSS metric computed over the calibration period, i.e. the odd years of the 2003-2016 period (Figure 6). Generally, the model performance increases with model complexity, i.e. the HSS is lowest for TI and highest for ETIB. All four models are more sensitive to Z_{\max} than the SWE_0 parameter. The mean optimal SWE_0 varies between 3 mm for TI to 6 mm for ETIB, with little variations in HSS score within this range as well as within each model. A mean optimal SWE_0 value of 4 mm was thus used for validation on even years and for further inter-model comparisons. This value is small compared to the 40 mm threshold used by Baba et al. (2019) and Gascoïn et al. (2015) but SWE_0 is resolution dependent, increasing with pixel resolution. The optimal Z_{\max} shows more variability between models, increasing with model complexity, i.e. lowest for TI and highest for ETIB. This is in fact to be expected from this parameter, which should also partly correct errors in ablation. A mean Z_{\max} of 1000m, which is within the zone of maximum performance for each model (Figure 6), was used for validation across models and for further inter-model comparisons.

Table 6 summarizes the calibration and validation metrics using the optimal parameter sets of each model and the mean optimal parameters. Generally, HSS increases slightly with model complexity, where the enhanced ETI (A&B) perform slightly better than the simpler TI and HTI models. Choosing the multi-model average parameter set over the model-specific optimal parameters affects little the performance in validation (Table 6a, b). In fact, some increases in performance are even noted, which suggest that the model-specific values may be slightly overfitted and less transferable compared to the multi-model average parameters. The slight overall differences in performance between models suggest that, on average, all models have similar abilities

to classify snow vs. snow free MODIS pixels, as assessed by the HSS metric. The small differences could be partly attributed to the fact that performance metrics are averaged over the whole calibration period. Hence, interannual and seasonal differences in model performance are investigated next.

Basin-wide SWE and SCA

Time series of daily simulated basin-wide SWE and fractional snow cover (fSCA) show significant intra and inter-annual variability over the period (2003-2016) (Figure 7). The fSCA simulated by the four models are in good agreement overall with MODIS observations, both in terms of timing and magnitude. In some years, however, the simulated snow covers lasts longer than observed in MODIS (2004, 2007, 2008, 2009, and 2012). These years had above average basin-wide simulated SWE (Figure 7a), so that overestimated accumulation in the upper basin during these wetter years could be the cause for the longer-lasting simulated SCA. In contrast, in years with scarce snowfall and thinner simulated snowpack (e.g. 2011, 2013, 2014, and 2016), the agreement between simulated and observed fSCA is better.

All four models show slight differences in their basin-wide fSCA and SWE predictions. Error metrics for the whole period (2003-2016) show that increasing model complexity slightly improves the correlation (r) and predictive skill (NSE) for basin-wide fSCA (Figure 7c). Both the root mean squared error (RMSE) and mean absolute error (MAE) also decrease with model complexity, but a larger bias for the ETIB model slightly increases its overall error relative to the ETIA model (Figure 7d). Hence, overall, the best performance is primarily observed for both enhanced radiative models ETIA and ETIB followed by the HTI and the classical TI models. Still, given the slight differences between models and the increased computational cost associated with enhanced radiative models, it is tempting to conclude at this point that the simplest temperature-based TI model offers a satisfactory performance to simulate SWE for hydrological applications in the High Atlas range. The causes for inter-model differences in model performance and in simulated SWE and melt are explored in the next sections.

Seasonality

The seasonality of the simulated SWE and fSCA was investigated to better understand seasonal inter-model differences (Figure 8). Models with a radiation term (HTI, ETIA, and ETIB) were contrasted to the classical TI model to highlight the effect of the different radiation terms to the simulated snow cover and model performance relative to MODIS (Figure 8d-f). The mean basin SWE seasonal cycle calculated over snow-covered areas only shows similar variations among models, particularly during the accumulation season (October-March) (Figure 8a). The mean simulated peak occurs in April and varies from 172 mm to 195 mm between models. Increasing differences between the ETI models and TI from March to May indicates increasing ablation rates simulated by these models relative to TI, while the HTI model differs significantly from TI only from May onward (Figure 8d). Maximum differences are reached at peak SWE in April for ETIA (-24 mm) and ETIB (-14 mm) and in June for HTI (-21 mm) (Figure 8d). When considering mean SWE over the whole basin surface, differences between the enhanced models and TI are more positive during winter and occur at different times. ETIB stands out with the largest mean peak SWE of 37 mm in March, following by HTI and the other models. In contrast to the classical TI, all radiative models simulate higher mean basin SWE in accumulation, while ETIA and HTI simulate lower SWE in late spring compared to TI.

The different seasonal behaviours in the mean basin SWE ($\text{SWE}_{\text{basin}}$) and mean SWE over snow covered areas (SWE_{SCA}) can be explained by differences in simulated SCA, since $\text{SWE}_{\text{basin}} = \text{fSCA} / 100 \times \text{SWE}_{\text{SCA}}$. All models, except ETIB, underestimated MODIS fSCA during accumulation, whereas all models overestimated MODIS fSCA during the ablation period, by 4.2% for ETIB and TI, and by 3.4% for HTI and ETIA (Figure 8c, f). This confirms the tendency identified in Figure 7 for wet years to have a longer-lasting snow cover simulated by all models, relative to MODIS. Inter-model differences show that all enhanced models simulate a larger snow cover than TI during the accumulation period, with ETIB being the most different and also most in line with MODIS, followed by HTI and ETIA. This explains the positive differences in $\text{SWE}_{\text{basin}}$ between these models and TI during the accumulation period (Figure 8b, e).

Seasonal variations in SCA model performance, as measured by the HSS index, were investigated over the calibration, validation, and entire period (Figure 9a-c). Globally, the HSS metric is highest ($\sim 0.6-0.75$) during winter and spring (December-April) but decreases sharply during the shoulder season (Oct.-Nov. and May-June). This shows that the model performance is generally good during most of the snow season, but that classification errors increase when the snow cover is restricted in the basin. All radiative models performed better than TI especially in the accumulation period, with ETIB performing best, with a maximum increase in HSS of 0.05 in calibration and 0.03 for both the validation and entire period. The models become gradually more similar in late spring (May-June).

Spatial performance

Model performance in predicting spatial variations in SCA was investigated by plotting the HSS metric against elevation bins (Figure 10). Overall, the HSS index increases with elevation for all models (Figure 10b). The mean fractional snow cover area (fSCA) also increases with elevation, in line with MODIS fSCA, but all models start overestimating fSCA above 3500 m (Figure 10a). The lowest HSS values are thus associated with the marginal and transient snow conditions found at the lowest elevations of the basin. Since these elevation areas represent a large share of the basin hypsometry (Figure 10a), the increased classification errors in these areas have a large influence on the basin-wide and time-averaged performance metrics displayed on Figure 6 and Table 6.

All enhanced models perform generally better than TI, although the gains in performance remain overall small (Figure 10c-e). Elevation trends also differ between the radiative models. ETIB performs best, but the improvement is most pronounced at lower elevations ($Z < 3000\text{m}$), which represent a large portion of the total basin but where there is less snow present throughout the year (Figure 10a). At high elevations ($Z > 3000\text{m}$) where mean SCA is above 30%, the gain in performance becomes more marginal for ETIB, while it is somewhat more pronounced for HTI and ETIA. While the bulk of the elevation bands show increased performance relative to TI, a small portion of grid points, in some cases up to of $\sim 20\%$ (left side of boxes in Figure 10 boxplots), suffered increased errors relative to TI.

Further insights into the performance behavior between models can be obtained by looking at classification success (TPR, TNR) and error (FPR, FNR) rates by altitude (Figure 11). Overall, TPR increases with elevation, reaching a maximum value of ~ 0.9 around 3600 m. (Figure 11, row 1). The enhanced models better classify snow presence than TI in the more transient snow zones ($\sim 1500-3200\text{m}$), with ETIB clearly performing best. The improvement for HTI is small but rather consistent with altitude, whereas ETIA shows more variations with even losses in performance in the highest and lowest altitudes relative to TI. Opposite to TPR, the true negative rate (TNR) decreases with altitude. Both ETI models show the largest deviations with TI, but decreased accuracy is seen at medium elevations, especially for ETIB (Figure 11, row 2). The elevation profile of the FPR error rate shows that all models tend to over predict snow presence towards higher altitudes (Figure 11, rows 3). Conversely, models rarely overpredict snow-free conditions at high elevations, but do so at the lower altitudes (Figure 11, rows 4). Enhanced models can be seen to reduce both the FPR and FNR errors on average, but large scatter occurs within elevation bands. The clearer improvement relative to TI is the decreased FNR error for ETIB (Figure 11d, rows 4).

Snow cover duration (SCD)

The simulated snow cover duration (SCD) was also compared to the observed SCD from MODIS (Figure 12) during calibration (odd years) and validation (even years). The radiative models that include global radiation (ETIA) and albedo (ETIB), slightly outperform ($r = 0.96$, $\text{RMSE} = 17$ days) the HTI and TI models ($r = 0.95$, $\text{RMSE} = 18-19$ days) in validation. Overall ETIB performed best, with lowest RMSE in calibration and in validation (equal to ETIA) and lower bias in validation. However, differences between models do not stand out clearly for SCD, despite significant spatial differences in SCA predictions and errors between models (Figure 10, Figure 11).

Discussion and conclusions

Difference in model performance

The enhanced radiative models, especially ETIB, showed increased performance relative to the simplest TI model for predicting basin wide SCA over time (Figure 7). In particular, the peak SCA in February was notably better simulated by the ETIB model compared to the other models (Figure 8c). However, overall differences in model performance were small. More contrasts between models were found in their ability to simulate the spatial heterogeneity of the snow cover. While all radiative models improved SCA predictions, the ETIB model showed the most improvement, with the largest gains in performance at mid to low elevations (Figure 10). The increasing FPR and decreasing FNR with elevations suggest that there may be a persistent elevation bias in the simulated SCA (Figure 11), which is partly alleviated by radiative models, in particular ETIB. This suggests that increasing global radiation with altitude (due to higher atmospheric transmissivity) and the consideration of snow albedo result in steeper ablation elevation profiles relative to temperature-only melt calculations with the TI model. However, the remaining elevation trends in the error rates point to lingering problems with the distribution of precipitation in the basin.

The distribution of precipitation in mountainous areas is challenging (Gottardi et al., 2012; Grunewald, Buhler, & Lehning, 2014; Nepal, Krause, Flugel, Fink, & Fischer, 2014), especially in a data-scarce regions such as the High Atlas Range. The exclusion of two high elevation stations with unreliable unheated tipping bucket gauges left us to rely heavily on the CAF station to extrapolate precipitations to higher elevations. While reliable, this station is located near the basin boundary and its elevation (2612 m) is low compared to the considerable amount of snow-covered terrain higher up (Figure 10a). Furthermore, the precipitation lapse rate calculated using the available stations up to 2612 m was found to be poorly defined due to the large spatial and temporal heterogeneity of observed precipitation, which prompted the decision to use a single and constant non-linear lapse rate calibrated on positive SWE changes at the Oukaimeden station (3230 m). The use of a calibrated maximum difference elevation (Z_{\max}) to limit the vertical extrapolation of precipitation may have limited the errors associated with this approach, but better spatially-distributed precipitation fields would be needed in the future to improve snow simulations for hydrological model applications. Outputs from numerical weather models are increasingly used for this purpose, but are still problematic for precipitation (Bellaire, Jamieson, & Fierz, 2011; Reveillet et al., 2020). Scaling precipitation inputs by measured snow distributions is another promising approach but requires costly airborne surveys to acquire reliable snow depth maps (Vogeli, Lehning, Wever, & Bavay, 2016). Progresses in mapping snow depth from high-resolution stereoscopic satellites images could however open new avenues on this front (Marti et al., 2016). Assimilation of snow cover maps within snow models can also help reducing precipitations biases, but increases computation costs (Baba et al., 2018; Margulis, Cortes, Giroto, & Durand, 2016).

Our results show that most of the snow cover variability is driven by elevation and that this trend was adequately captured by all four models (Figure 10). Hence the simple TI model could be sufficient for melt simulations at the basin scale, due to the strong dependence of temperature and related melt rates on elevation, as found elsewhere (e.g. Hock, 2003; Reveillet et al., 2017; Vincent, 2002). The enhanced radiative models improved the snow cover simulations, but given their significant extra computational cost, our results suggest that the simpler TI is adequate for operational snow simulations in the high Atlas Range. This contrasts previous studies that showed that including solar radiation improves the performance of spatially-distributed melt models for predictions of glacier mass balance (Gabbi et al., 2014), snow cover area (Follum, Downer, Niemann, Roylance, & Vuyovich, 2015) and streamflow from snow-fed basins (Brubaker, Rango, & Kustas, 1996; Follum, Niemann, & Fassnacht, 2019). On the other hand, the use of a fully distributed (grid-based) model improved the simulations of SCA relative to semi-distributed temperature index models previously applied in this basin (Boudhar et al., 2009).

Despite the overall good performance for the simple TI model, enhanced models still explained more variability in SCA per elevation band, but with notable discrepancies among models (Figure 10). To better

understand these discrepancies, the simulated SWE and melt rates were compared by elevation band (Figure 13). The HTI model shows the smallest difference relative to TI, in line with its more similar performance in SCA simulations. This can be attributed to the fact that HTI only considers the potential clear-sky radiation and thus ignores temporal variations in atmospheric transmissivity and albedo. Both ETI models show significant differences in simulated SWE (Figure 13c, d) and melt rates (Figure 13g, h) relative to TI. The best performing ETIB model simulates smaller melt rates and larger SWE at middle elevations (2000-3500 m), and higher melt rates and smaller SWE at the highest elevations (>3500 m). Interestingly, median differences in SWE and melt rates per elevation band are rather small, which again shows that the preponderant influence of elevation on the simulated SWE is well captured by the simple TI model. However, significant deviations occur, up to ca. $+20$ mm for SWE and ca. $+1$ mm d^{-1} for melt rates (Figure 13c-d, g-h). Even more interesting is the fact that these significant differences in melt rates and SWE do not result in larger inter-model differences in SCA simulations. On the one hand, this shows the general limitation of using satellite SCA to validate and compare model performance for SWE simulations. On the other hand, it also points to possible adverse effect of using coarse resolution products such as MODIS for validation of higher-resolution models. This topic is discussed in detail next.

Effect of resolution on SCA validation

In order to compare the simulated SCA with MODIS, the modelled SCA was aggregated from 100 m to the 500 m resolution of MODIS (Figure 3). This has the potential to suppress significant spatial variability in the finer (100 m) scale simulated SCA. To explore this, the snow cover duration (SCD, equal to mean SCA \times 365 days) modelled at the original 100 m resolution was compared to that aggregated at 500 m resolution (Figure 14). While the overall elevation trends remain unchanged, the aggregation of SCA from 100 m to 500 m results in significant changes in SCA at some elevations, especially for the ETI models (Figure 14c-d vs. g-h). The simulated median SCD elevation profiles at 500 m resolution are not as smooth as the original ones at 100 m (Figure 14a vs. e). This is explained by the considerable smoothing of SCA variability related to slope and aspect variations at scales finer than 500 m, as seen by the considerable noise in the median northern exposure index profile for the 500 m aggregated vs. original 100 m DEM (Figure 14a vs. e). This loss, upon aggregation, of topographic-induced SCA variability simulated by the radiative models can partly explain why the SCD simulated at 500 m by the different models give overall similar results compared to MODIS (Figure 12, Figure 14i-l).

The smoothing effect of model aggregation is particularly evident when plotting modelled quantities (SWE, melt rates and SCD) by aspect (Figure 15). At the original 100 m model resolution, all radiative models expectedly simulate smaller melt rates and larger SWE on northern slopes, and vice-versa on southern slopes (Figure 15a, b), which results in longer-lasting snow on northern slopes compared to TI (Figure 15c). This is in line with previous studies (e.g. Baba et al., 2019; Comola et al., 2015; Lopez-Moreno & Stahli, 2008) which found that south-facing slopes receive more solar radiation and generally melts faster than on north-facing slopes. Aggregation of simulated SCA to 500 m results in significant disruption of this pattern (Figure 15d), which can be attributed to changes in the distribution of slopes and aspects following aggregation (Figure 15e). These results corroborate previous conclusions made by Baba et al. (2019) concerning the influence of DEM resolution on the simulation of snow cover. Using the physically-based model SnowModel (Liston & Elder, 2006a), they found a significant degradation of model performance when aggregating the model DEM to resolutions of 500 m and beyond, which disrupted the representation of slopes in the basin and affected solar radiation variability. Comola et al. (2015) also showed that the effects of solar radiation patterns on the hydrologic response of snow-covered basins are scale dependent, i.e., significant at small scales with predominant aspects and weak at larger scales where aspects become uncorrelated and orientation differences average out. They further found that a calibrated TI model on scales larger than the aspect correlation scale are well transferable. Their conclusions find support in our results: (i) the inclusion of radiation patterns in the large Rheraya catchment has a small influence overall on basin-wide simulated average SWE and SCA. (ii) The influence of solar radiation on simulated SWE and melt rates is greatly suppressed when aggregating model outputs to MODIS resolution of 500 m, which smooths out radiation effects and brings

the radiative models closer to simulations made with a simple temperature-based (TI) model. Our results support the notion that in large basins (i.e. larger than the correlation length of the terrain), topographic-induced variations in solar radiation tend to average out so that mean simulated melt rates, SWE and SCA do not differ greatly from using temperature alone to predict snowmelt. A more uniform distribution of slope aspects in a basin, such as observed here for Rheraya (cf. Figure 15), will reinforce this phenomenon. In the context of operational flow forecasting in the High Atlas Range, simple temperature index models will thus provide sufficiently accurate snowmelt estimates.

Our findings also call for caution when using medium resolution satellite products such as MODIS to validate spatially distributed snow models. The necessary aggregation of finer-scale model outputs to a resolution larger than key processes scales, such as that where interactions between topography and solar radiation are greatest, will suppress valid model information. The increasing availability of publicly available high-resolution snow cover maps imagery (Gascoin, Grizonnet, Bouchet, Salgues, & Hagolle, 2019) should progressively reduce our dependence on MODIS snow cover products and help crash-testing high-resolution snow models in the future.

Data availability statement

MODIS data that support the findings of this study are openly available in the National Snow and Ice Data Center (NSIDC) at (<https://nsidc.org/>), and meteorological data are upon demand with authors.

References

- Abudu, S., Cui, C.-l., Saydi, M., & King, J. P. (2012). Application of snowmelt runoff model (SRM) in mountainous watersheds: A review. *Water Science and Engineering*, 5 , 123-136. doi:10.3882/j.issn.1674-2370.2012.02.001
- Aguilar, C., Herrero, J., & Polo, M. J. (2010). Topographic effects on solar radiation distribution in mountainous watersheds and their influence on reference evapotranspiration estimates at watershed scale. *Hydrology and Earth System Sciences*, 14 (12), 2479-2494. doi:10.5194/hess-14-2479-2010
- Allen, R. G., Trezza, R., & Tasumi, M. (2006). Analytical integrated functions for daily solar radiation on slopes. *Agricultural and Forest Meteorology*, 139 (1-2), 55-73. doi:10.1016/j.agrformet.2006.05.012
- Alpert, P. (1986). Mesoscale indexing of the distribution of orographic precipitation over high mountains. *Journal of climate and applied meteorology*, 25 (4), 532-545.
- Anderton, S. P., White, S. M., & Alvera, B. (2004). Evaluation of spatial variability in snow water equivalent for a high mountain catchment. *Hydrological Processes*, 18 (3), 435-453. doi:10.1002/hyp.1319
- Arsenault, R., Brissette, F., & Martel, J.-L. (2018). The hazards of split-sample validation in hydrological model calibration. *Journal of Hydrology*, 2018 v.566 , pp. 346-362. doi:10.1016/j.jhydrol.2018.09.027
- Baba, M. W., Gascoin, S., Jarlan, L., Simonneaux, V., & Hanich, L. (2018). Variations of the Snow Water Equivalent in the Ourika Catchment (Morocco) over 2000–2018 Using Downscaled MERRA-2 Data. *Water*, 10 (9), 1120. doi:10.3390/w10091120
- Baba, M. W., Gascoin, S., Kinnard, C., Marchane, A., & Hanich, L. (2019). Effect of Digital Elevation Model Resolution on the Simulation of the Snow Cover Evolution in the High Atlas. *Water Resources Research*, 55 (7), 5360-5378. doi:10.1029/2018wr023789
- Bair, E. H., Rittger, K., Davis, R. E., Painter, T. H., & Dozier, J. (2016). Validating reconstruction of snow water equivalent in California’s Sierra Nevada using measurements from the NASA Airborne Snow Observatory. *Water Resources Research*, 52 (11), 8437-8460. doi:10.1002/2016wr018704

- Barnes, S. L. (1964). A technique for maximizing details in numerical weather map analysis. *Journal of Applied Meteorology*, 3 (4), 396-409.
- Barnett, T. P., Adam, J. C., & Lettenmaier, D. P. (2005). Potential impacts of a warming climate on water availability in snow-dominated regions. *Nature*, 438 (7066), 303-309. doi:10.1038/nature04141
- Bellaire, S., Jamieson, J. B., & Fierz, C. (2011). Forcing the snow-cover model SNOWPACK with forecasted weather data. *The Cryosphere*, 5 (4), 1115-1125. doi:10.5194/tc-5-1115-2011
- Bouamri, H., Boudhar, A., Gascoin, S., & Kinnard, C. (2018). Performance of temperature and radiation index models for point-scale snow water equivalent (SWE) simulations in the Moroccan High Atlas Mountains. *Hydrological Sciences Journal*, 63 (12), 1844-1862. doi:10.1080/02626667.2018.1520391
- Boudhar, A., Boulet, G., Hanich, L., Sicart, J. E., & Chehbouni, A. (2016). Energy fluxes and melt rate of a seasonal snow cover in the Moroccan High Atlas. *Hydrological Sciences Journal*, 61 , 931-943. doi:10.1080/02626667.2014.965173
- Boudhar, A., Duchemin, B., Hanich, L., Jarlan, L., Chaponniere, A., Maisongrande, P., . . . Chehbouni, A. (2010). Long-term analysis of snow-covered area in the Moroccan High-Atlas through remote sensing. *International Journal of Applied Earth Observation and Geoinformation*, 12 , S109-S115. doi:10.1016/j.jag.2009.09.008
- Boudhar, A., Hanich, L., Boulet, G., Duchemin, B., Berjamy, B., & Chehbouni, A. (2009). Evaluation of the Snowmelt Runoff Model in the Moroccan High Atlas Mountains using two snow-cover estimates. *Hydrological Sciences Journal*, 54 , 1094-1113.
- Boudhar, A., Ouatiki, H., Bouamri, H., Lebrini, Y., Karaoui, I., Hssaisoune, M., . . . Benabdelouahab, T. (2020). Hydrological Response to Snow Cover Changes Using Remote Sensing over the Oum Er Rbia Upstream Basin, Morocco. In *Mapping and Spatial Analysis of Socio-economic and Environmental Indicators for Sustainable Development* (pp. 95-102): Springer.
- Brubaker, K., Rango, A., & Kustas, W. (1996). Incorporating radiation inputs into the snowmelt runoff model. *Hydrological Processes*, 10 , 1329-1343. doi:10.1002/(SICI)1099-1085(199610)10:10<1329::AID-HYP464>3.3.CO;2-N
- Carenzo, M., Pellicciotti, F., Rimkus, S., & Burlando, P. (2009). Assessing the transferability and robustness of an enhanced temperature-index glacier-melt model. *Journal of Glaciology*, 55 (190), 258-274.
- Chaponniere, A., Maisongrande, P., Duchemin, B., Hanich, L., Boulet, G., Escadafal, R., & Elouaddat, S. (2005). A combined high and low spatial resolution approach for mapping snow covered areas in the Atlas mountains. *International Journal of Remote Sensing*, 26 (13), 2755-2777. doi:10.1080/01431160500117758
- Chebouni, A., Escadafal, R., Duchemin, B., Boulet, G., Simonneaux, V., Dedieu, G., . . . Sobrino, J. a. (2008). An integrated modelling and remote sensing approach for hydrological study in arid and semi-arid regions: the SUDMED Programme. *International Journal of Remote Sensing*, 29 , 5161-5181. doi:10.1080/01431160802036417
- Cohen, J. (1960). A coefficient of agreement for nominal scales. *Educational and psychological measurement*, 20 (1), 37-46.
- Collados-Lara, A. J., Pardo-Iguzquiza, E., Pulido-Velazquez, D., & Jimenez-Sanchez, J. (2018). Precipitation fields in an alpine Mediterranean catchment: Inversion of precipitation gradient with elevation or undercatch of snowfall? *International Journal of Climatology*, 38 (9), 3565-3578.
- Comola, F., Schaeffli, B., Ronco, P. D., Botter, G., Bavay, M., Rinaldo, A., & Lehning, M. (2015). Scale-dependent effects of solar radiation patterns on the snow-dominated hydrologic response. *Geophysical Research Letters*, 42 (10), 3895-3902.

- De Jong, C., Lawler, D., & Essery, R. (2009). Mountain hydroclimatology and snow seasonality - Perspectives on climate impacts, snow seasonality and hydrological change in mountain environments. *Hydrological Processes*, 23 , 955-961. doi:10.1002/hyp.7193
- Eeckman, J., Chevallier, P., Boone, A., Neppel, L., De Rouw, A., Delclaux, F., & Koirala, D. (2017). Providing a non-deterministic representation of spatial variability of precipitation in the Everest region. *Hydrology and Earth System Sciences*, 21 (9), 4879-4893. doi:10.5194/hess-21-4879-2017
- Fassnacht, S. R., Lopez-Moreno, J., Ma, C., Weber, A., Pfohl, A., Kampf, S., & Kappas, M. (2017). Spatio-temporal snowmelt variability across the headwaters of the Southern Rocky Mountains. *Frontiers of Earth Science*, 11 (3), 505-514.
- Fassnacht, S. R., Venable, H. N. B., Khishigbayar, J., & Cherry, M. (2013). The probability of precipitation as snow derived from daily air temperature for high elevation areas of Colorado, United States.
- Fayad, A., Gascoïn, S., Faour, G., Lopez-Moreno, J. I., Drapeau, L., Le Page, M., & Escadafal, R. (2017). Snow hydrology in Mediterranean mountain regions: A review. *Journal of Hydrology*, 551 , 374-396.
- Feiccabrino, J., Graff, W., Lundberg, A., Sandstrom, N., & Gustafsson, D. (2015). Meteorological Knowledge Useful for the Improvement of Snow Rain Separation in Surface Based Models. *Hydrology*, 2 (4), 266-288. doi:10.3390/hydrology2040266
- Follum, M. L., Downer, C. W., Niemann, J. D., Roylance, S. M., & Vuyovich, C. M. (2015). A radiation-derived temperature-index snow routine for the GSSHA hydrologic model. *Journal of Hydrology*, 529 , 723-736. doi:10.1016/j.jhydrol.2015.08.044
- Follum, M. L., Niemann, J. D., & Fassnacht, S. R. (2019). A comparison of snowmelt-derived streamflow from temperature-index and modified-temperature-index snow models. *Hydrological Processes*, 33 (23), 3030-3045. doi:10.1002/hyp.13545
- Gabbi, J., Carenzo, M., Pellicciotti, F., Bauder, A., & Funk, M. (2014). A comparison of empirical and physically based glacier surface melt models for long-term simulations of glacier response. *Journal of Glaciology*, 60 (224), 1140-1154. doi:10.3189/2014JoG14J011
- Gafurov, A., & Bardossy, A. (2009). Cloud removal methodology from MODIS snow cover product. *Hydrology and Earth System Sciences*, 13 (7), 1361-1373.
- Gao, Y., Xie, H., Yao, T., & Xue, C. (2010). Integrated assessment on multi-temporal and multi-sensor combinations for reducing cloud obscuration of MODIS snow cover products of the Pacific Northwest USA. *Remote Sensing of Environment*, 114 (8), 1662-1675. doi:10.1016/j.rse.2010.02.017
- Gascoïn, S., Grizonnet, M., Bouchet, M., Salgues, G., & Hagolle, O. (2019). Theia Snow collection: high-resolution operational snow cover maps from Sentinel-2 and Landsat-8 data. *Earth System Science Data*, 11 (2), 493-514. doi:10.5194/essd-11-493-2019
- Gascoïn, S., Hagolle, O., Huc, M., Jarlan, L., Dejoux, J. F., Szczypta, C., . . . Sanchez, R. (2015). A snow cover climatology for the Pyrenees from MODIS snow products. *Hydrology and Earth System Sciences*, 19 (5), 2337-2351. doi:10.5194/hess-19-2337-2015
- Gottardi, F., Obled, C., Gailhard, J., & Paquet, E. (2012). Statistical reanalysis of precipitation fields based on ground network data and weather patterns: Application over French mountains. *Journal of Hydrology*, 432-433 , 154-167. doi:10.1016/j.jhydrol.2012.02.014
- Grunewald, T., Buhler, Y., & Lehning, M. (2014). Elevation dependency of mountain snow depth. *The Cryosphere*, 8 (6), 2381-2394.
- Grunewald, T., Schirmer, M., Mott, R., & Lehning, M. (2010). Spatial and temporal variability of snow depth and ablation rates in a small mountain catchment. *The Cryosphere*, 4 (2), 215-225. doi:10.5194/tc-4-215-2010

- Hajhouji, Y., Simonneaux, V., Gascoin, S., Fakir, Y., Richard, B., Chehbouni, A., & Boudhar, A. (2018). Modelisation pluie-debit et analyse du regime d'un bassin versant semi-aride sous influence nivale. Cas du bassin versant du Rheraya (Haut Atlas, Maroc). *La Houille Blanche* (3), 49-62. doi:10.1051/lhb/2018032
- Hall, D. K., & Riggs, G. A. (2016). MODIS/Terra Snow Cover Daily L3 Global 0.05 Deg CMG, Version 6, NASA National Snow and Ice Data Center Distributed Active Archive Center, Boulder, Colorado, USA. In.
- Hall, D. K., Riggs, G. A., & Salomonson, V. V. (1995). Development of methods for mapping global snow cover using moderate resolution imaging spectroradiometer data. *Remote Sensing of Environment*, 54 (2), 127-140.
- Han, P., Long, D., Han, Z., Du, M., Dai, L., & Hao, X. (2019). Improved understanding of snowmelt runoff from the headwaters of China's Yangtze River using remotely sensed snow products and hydrological modeling. *Remote Sensing of Environment*, 224 , 44-59. doi:10.1016/j.rse.2019.01.041
- Heidke, P. (1926). Berechnung des Erfolges und der Gute der Windstarkevorhersagen im Sturmwarnungsdienst. *Geografiska Annaler*, 8 (4), 301-349.
- Herrero, J., Polo, M. J., Monino, A., & Losada, M. A. (2009). An energy balance snowmelt model in a Mediterranean site. *Journal of Hydrology*, 371 (1-4), 98-107. doi:10.1016/j.jhydrol.2009.03.021
- Hock, R. (1999). A distributed temperature-index ice-and snowmelt model including potential direct solar radiation. *Journal of Glaciology*, 45 (149), 101-111.
- Hock, R. (2003). Temperature index melt modelling in mountain areas. *Journal of Hydrology*, 282 , 104-115. doi:10.1016/S0022-1694(03)00257-9
- Homan, J. W., Luce, C. H., McNamara, J. P., & Glenn, N. F. (2011). Improvement of distributed snowmelt energy balance modeling with MODIS-based NDSI-derived fractional snow-covered area data. *Hydrological Processes*, 25 (4), 650-660. doi:10.1002/hyp.7857
- Hublart, P., Ruelland, D., Cortazar-atauri, I. G. D., Gascoin, S., Lhermitte, S., & Ibacache, A. (2016). Reliability of lumped hydrological modeling in a semi-arid mountainous catchment facing water-use changes. *Hydrology and Earth System Sciences*, 20 , 3691-3717. doi:10.5194/hess-20-3691-2016
- Jarlan, L., Khabba, S., Er-Raki, S., Le Page, M., Hanich, L., Fakir, Y., . . . Escadafal, R. (2015). Remote sensing of water resources in semi-arid mediterranean areas: the joint international laboratory TREMA. *International Journal of Remote Sensing*, 36 , 4879-4917. doi:10.1080/01431161.2015.1093198
- Kampf, S. K., & Richer, E. E. (2014). Estimating source regions for snowmelt runoff in a Rocky Mountain basin: tests of a data-based conceptual modeling approach. *Hydrological Processes*, 28 (4), 2237-2250. doi:10.1002/hyp.9751
- Lehning, M., Volksch, I., Gustafsson, D., Nguyen, T. A., Stahli, M., & Zappa, M. (2006). ALPINE3D: a detailed model of mountain surface processes and its application to snow hydrology. *Hydrological Processes*, 20 (10), 2111-2128. doi:10.1002/hyp.6204
- Letsinger, S. L., & Olyphant, G. A. (2007). Distributed energy-balance modeling of snow-cover evolution and melt in rugged terrain: Tobacco Root Mountains, Montana, USA. *Journal of Hydrology*, 336 (1-2), 48-60. doi:10.1016/j.jhydrol.2006.12.012
- Liston, G. E., & Elder, K. (2006a). A Distributed Snow-Evolution Modeling System (SnowModel). *Journal of Hydrometeorology*, 7 .
- Liston, G. E., & Elder, K. (2006b). A meteorological distribution system for high-resolution terrestrial modeling (MicroMet). *Journal of Hydrometeorology*, 7 (2), 217-234.
- Lopez-Moreno, J. I., Gascoin, S., Herrero, J., Sproles, E. A., Pons, M., Alonso-Gonzalez, E., . . . Pomeroy, J. (2017). Different sensitivities of snowpacks to warming in Mediterranean climate mountain

areas. *Environmental Research Letters*, 12 .

- Lopez-Moreno, J. I., & Stahli, M. (2008). Statistical analysis of the snow cover variability in a subalpine watershed: Assessing the role of topography and forest interactions. *Journal of Hydrology*, 348 (3-4), 379-394. doi:10.1016/j.jhydrol.2007.10.018
- Magand, C., Ducharne, A., Le Moine, N., & Gascoïn, S. (2014). Introducing Hysteresis in Snow Depletion Curves to Improve the Water Budget of a Land Surface Model in an Alpine Catchment. *Journal of Hydrometeorology*, 15 (2), 631-649. doi:10.1175/jhm-d-13-091.1
- Marchane, A., Jarlan, L., Hanich, L., Boudhar, A., Gascoïn, S., Tavernier, A., . . . Berjamy, B. (2015). Assessment of daily MODIS snow cover products to monitor snow cover dynamics over the Moroccan Atlas mountain range. *Remote Sensing of Environment*, 160 , 72- 86. doi:10.1016/j.rse.2015.01.002
- Margulis, S. A., Cortes, G., Giroto, M., & Durand, M. (2016). A Landsat-Era Sierra Nevada Snow Reanalysis (1985–2015). *Journal of Hydrometeorology*, 17 (4), 1203-1221. doi:10.1175/jhm-d-15-0177.1
- Marks, D., Winstral, A., Reba, M., Pomeroy, J., & Kumar, M. (2013). An evaluation of methods for determining during-storm precipitation phase and the rain/snow transition elevation at the surface in a mountain basin. *Advances in Water Resources*, 55 , 98-110. doi:10.1016/j.advwatres.2012.11.012
- Marti, R., Gascoïn, S., Berthier, E., de Pinel, M., Houet, T., & Laffly, D. (2016). Mapping snow depth in open alpine terrain from stereo satellite imagery. *The Cryosphere*, 10 (4), 1361-1380. doi:10.5194/tc-10-1361-2016
- Matin, M. A., & Bourque, C. P. A. (2013). Intra- and inter-annual variations in snow–water storage in data sparse desert–mountain regions assessed from remote sensing. *Remote Sensing of Environment*, 139 , 18-34. doi:10.1016/j.rse.2013.07.033
- Mazurkiewicz, A. B., Callery, D. G., & McDonnell, J. J. (2008). Assessing the controls of the snow energy balance and water available for runoff in a rain-on-snow environment. *Journal of Hydrology*, 354 (1-4), 1-14. doi:10.1016/j.jhydrol.2007.12.027
- McCabe, G., & Wolock, D. (1999). Future snowpack conditions in the western United States derived from general circulation model climate simulations. *Journal of the American Water Resources Association*, 35 (1), 473-471,484.
- Molotch, N. P., Colee, M. T., Bales, R. C., & Dozier, J. (2005). Estimating the spatial distribution of snow water equivalent in an alpine basin using binary regression tree models: the impact of digital elevation data and independent variable selection. *Hydrological Processes*, 19 (7), 1459-1479. doi:10.1002/hyp.5586
- Moore, R., Trubilowicz, J., & Buttle, J. (2012). Prediction of Streamflow Regime and Annual Runoff for Ungauged Basins Using a Distributed Monthly Water Balance Model 1. *JAWRA Journal of the American Water Resources Association*, 48 (1), 32-42.
- Nepal, S., Krause, P., Flugel, W. A., Fink, M., & Fischer, C. (2014). Understanding the hydrological system dynamics of a glaciated alpine catchment in the Himalayan region using the J2000 hydrological model. *Hydrological Processes*, 28 (3), 1329-1344. doi:10.1002/hyp.9627
- Notarnicola, C., Duguay, M., Moelg, N., Schellenberger, T., Tetzlaff, A., Monsorno, R., . . . Zebisch, M. (2013). Snow Cover Maps from MODIS Images at 250 m Resolution, Part 2: Validation. *Remote Sensing*, 5 (4), 1568-1587. doi:10.3390/rs5041568
- Olyphant, G. A. (1984). Insolation topoclimates and potential ablation in alpine snow accumulation basins: Front Range, Colorado. *Water Resources Research*, 20 (4), 491-498.
- Parajka, J., & Blöschl, G. (2008). The value of MODIS snow cover data in validating and calibrating conceptual hydrologic models. *Journal of Hydrology*, 358 (3-4), 240-258. doi:10.1016/j.jhydrol.2008.06.006

- Parajka, J., & Blöschl, G. (2012). MODIS-based snow cover products, validation, and hydrologic applications. *Multiscale Hydrologic Remote Sensing: Perspectives and Applications*, edited by: Chang, N.-B. and Hong, Y .
- Pellicciotti, F., Brock, B., Strasser, U., Burlando, P., Funk, M., & Corripio, J. (2005). An enhanced temperature-index glacier melt model including the shortwave radiation balance : development and testing for Haut Glacier d’Arolla, Switzerland. *Journal of Glaciology*, 51 , 573-587. doi:10.3189/172756505781829124
- Pimentel, R., Herrero, J., & Polo, M. (2017). Quantifying Snow Cover Distribution in Semiarid Regions Combining Satellite and Terrestrial Imagery. *Remote Sensing*, 9 (10). doi:10.3390/rs9100995
- Reveillet, M., MacDonell, S., Gascoïn, S., Kinnard, C., Lhermitte, S., & Schaffer, N. (2020). Impact of forcing on sublimation simulations for a high mountain catchment in the semiarid Andes. *The Cryosphere*, 14 (1), 147-163. doi:10.5194/tc-14-147-2020
- Reveillet, M., Vincent, C., Six, D., & Rabatel, A. (2017). Which empirical model is best suited to simulate glacier mass balances? *Journal of Glaciology*, 63 (237), 39-54. doi:10.1017/jog.2016.110
- Riggs, G. A., & Hall, D. K. (2004). *Snow mapping with the MODIS Aqua instrument*. Paper presented at the Proceedings of the 61st Eastern Snow Conference, Portland, ME, USA.
- Riggs, G. A., Hall, D. K., & Roman, M. O. (2016). VIIRS Snow Cover Algorithm Theoretical Basis Document (ATBD). *NASA VIIRS project document* [<https://modis-snowice.gsfc.nasa.gov> .
- Rittger, K., Painter, T. H., & Dozier, J. (2013). Assessment of methods for mapping snow cover from MODIS. *Advances in Water Resources*, 51 , 367-380. doi:10.1016/j.advwatres.2012.03.002
- Rochdane, S., Reichert, B., Messouli, M., Babqiqi, A., & Khebiza, M. Y. (2012). Climate Change Impacts on Water Supply and Demand in Rheraya Watershed (Morocco), with Potential Adaptation Strategies. *Water*, 4 (4), 28-44. doi:10.3390/w4010028
- Roe, G. H., & Baker, M. B. (2006). Microphysical and geometrical controls on the pattern of orographic precipitation. *Journal of the Atmospheric Sciences*, 63 (3), 861-880.
- Salomonson, V. V., & Appel, I. (2006). Development of the Aqua MODIS NDSI fractional snow cover algorithm and validation results. *IEEE Transactions on Geoscience and Remote Sensing*, 44 (7), 1747-1756.
- Schneider, C., Kilian, R., & Glaser, M. (2007). Energy balance in the ablation zone during the summer season at the Gran Campo Nevado Ice Cap in the Southern Andes. *Global and Planetary Change*, 59 , 175-188. doi:10.1016/j.gloplacha.2006.11.033
- Schulz, O., & de Jong, C. (2004). Snowmelt and sublimation : field experiments and modelling in the High Atlas Mountains of Morocco *Hydrology and Earth System Sciences*, 8 (6), 1076-1086.
- Senzeba, K. T., Bhadra, A., & Bandyopadhyay, A. (2015). Snowmelt runoff modelling in data scarce Nuranang catchment of eastern Himalayan region. *Remote Sensing Applications: Society and Environment*, 1 , 20-35. doi:10.1016/j.rsase.2015.06.001
- Singh, P., & Bengtsson, L. (2003). Effect of warmer climate on the depletion of snow-covered area in the Satluj basin in the western Himalayan region. *Hydrological Sciences Journal*, 48 (3), 413-425. doi:10.1623/hysj.48.3.413.45280
- Tarboton, D. G., & Luce, C. H. (1996). Utah Energy Balance Snow Accumulation and Melt Model (UEB). Utah Water Research Laboratory Utah State University.
- Vicuna, S., Garreaud, R. D., & McPhee, J. (2011). Climate change impacts on the hydrology of a snowmelt driven basin in semiarid Chile. *Climatic Change*, 105 (3-4), 469-488. doi:10.1007/s10584-010-9888-4
- Vincent, C. (2002). Influence of climate change over the 20th Century on four French glacier mass balances. *Journal of Geophysical Research*, 107 (D19). doi:10.1029/2001jd000832

- Viviroli, D., & Weingartner, R. (2008). “Water Towers”—A Global View of the Hydrological Importance of Mountains. In E. Wiegandt (Ed.), *Mountains: Sources of Water, Sources of Knowledge* (pp. 15-20). Dordrecht: Springer Netherlands.
- Vogeli, C., Lehning, M., Wever, N., & Bavay, M. (2016). Scaling Precipitation Input to Spatially Distributed Hydrological Models by Measured Snow Distribution. *Frontiers in Earth Science*, *4* (108). doi:10.3389/feart.2016.00108
- Wang, X., & Xie, H. (2009). New methods for studying the spatiotemporal variation of snow cover based on combination products of MODIS Terra and Aqua. *Journal of Hydrology*, *371* (1-4), 192-200. doi:10.1016/j.jhydrol.2009.03.028
- Willis, I. C., Arnold, N. S., & Brock, B. W. (2002). Effect of snowpack removal on energy balance , melt and runoff in a small supraglacial catchment. *Hydrological processes*, *16* , 2721-2749. doi:10.1002/hyp.1067
- Xiao, X., Zhang, Q., Boles, S., Rawlins, M., & Moore, B. (2004). Mapping snow cover in the pan-Arctic zone, using multi-year (1998-2001) images from optical VEGETATION sensor. *International Journal of Remote Sensing*, *25* (24), 5731-5744. doi:10.1080/01431160410001719867
- Xie, H., Wang, X., & Liang, T. (2009). Development and assessment of combined Terra and Aqua snow cover products in Colorado Plateau, USA and northern Xinjiang, China. *Journal of Applied Remote Sensing*, *3* (1), 033559.
- Xue, H., Wang, J., Xiao, Z., Chen, P., & Liu, Y. (2014). Combining MODIS and AMSR-E observations to improve MCD43A3 short-time snow-covered Albedo estimation. *Hydrological Processes*, *28* (3), 570-580. doi:10.1002/hyp.9570
- Yasutomi, N., Hamada, A., & Yatagai, A. (2011). Development of a long-term daily gridded temperature dataset and its application to rain/snow discrimination of daily precipitation. *Global Environmental Research*, *15* (2), 165-172.
- Zappa, M. (2008). Objective quantitative spatial verification of distributed snow cover simulations—an experiment for the whole of Switzerland / Verification quantitative spatiale objective de simulations distribuees de la couche de neige—une etude pour l’ensemble de la Suisse. *Hydrological Sciences Journal*, *53* (1), 179-191. doi:10.1623/hysj.53.1.179
- Zhang, H., Zhang, F., Zhang, G., Che, T., Yan, W., Ye, M., & Ma, N. (2019). Ground-based evaluation of MODIS snow cover product V6 across China: Implications for the selection of NDSI threshold. *Sci Total Environ*, *651* (Pt 2), 2712-2726. doi:10.1016/j.scitotenv.2018.10.128
- Zhou, H., Aizen, E., & Aizen, V. (2013). Deriving long term snow cover extent dataset from AVHRR and MODIS data: Central Asia case study. *Remote Sensing of Environment*, *136* , 146-162. doi:10.1016/j.rse.2013.04.015

Tables

Table 1: Characteristic and geographic coordinates (WGS-84) of weather stations in the Rheraya catchment, with available observations: precipitation (P), air temperature (T), relative humidity (RH), wind speed (WS), snowfall (S), shortwaves radiations (SR) and runoff (Q).

Stations	Latitude (°)	Latitude (°)	Longitude (°)	Longitude (°)	Elevation GPS (m)	Elevation GPS (m)	Elevation DEM (m)	Elevation DEM (m)	Z _{interp} (m)	Z _{interp} (m)
Aremd	31.12	-7.92	-7.92	1940	1940	1938	1938	2015	2015	P, T, RH, WS
Asni	31.25	-7.98	-7.98	1170	1170	1183	1183	1105	1105	P
Imskerbour	31.20	-7.94	-7.94	1404	1404	1426	1426	1931	1931	P, T, RH.
Neltner	31.07	-7.94	-7.94	3207	3207	3120	3120	1961	1961	P, T, RH, WS
Oukaimeden SM	31.18	-7.87	-7.87	3230	3230	3239	3239	2482	2482	P, T, RH, SR, WS
Tachedert	31.16	-7.94	-7.94	2343	2343	2321	2321	2467	2467	T, RH
Tamatarte	31.14	-7.90	-7.90	1924	1924	1913	1913	2119	2119	P
Matate	31.16	-7.85	-7.85	1825	1825	1800	1800	1997	1997	P
CAF	31.21	-7.86	-7.86	2612	2612	2635	2635	2515	2515	P, T, S
Tahanaout	31.29	-7.96	-7.96	925	925	1069	1069	986	986	P, Q

Z_{interp} interpolated weather station elevations at Rheraya catchment.

Table 2 : Melt models equations used in this study. Variables are defined in footnote and model parameters in Table 3.

Snowmelt models	Equations
Classical temperature index (TI) melt model	$M = \begin{cases} \text{DDF} \times T_a & T_a > T_T \\ 0 & T_a \leq T_T \end{cases}$
Hock's temperature index melt model (HTI)	$M = \begin{cases} (\text{MF} + \text{RF} \times I_{\text{pot}}) T_a & T_a > T_T \\ 0 & T_a \leq T_T \end{cases}$
Enhanced temperature-index (ETIA) melt model	$(4a) I_{\text{pot}} = I_0 \left(\frac{R_m}{R} \right) \times \psi \alpha \left(\frac{P}{P_0 \cos Z} \right) \times \cos \theta \quad (4b)$ $M = \begin{cases} \text{TF} \times T_a + \text{SRF}_{\text{in}} \times I & T_a > T_T \\ 0 & T_a \leq T_T \end{cases}$ $(5a) R = -0.000054 \times \text{RH}^2 - 0.0024 \times \text{RH} + 1.3$ $(5b) I = R \times I_{\text{pot}} \quad (5c)$

Snowmelt models	Equations
Enhanced temperature-index (ETIB) melt model	$M = \begin{cases} TF \times T_a + SRF_{\text{net}} (1 - \alpha) I & T_a > T_T \\ 0 & T_a \leq T_T \end{cases}$ $(6a) \quad \alpha = p_1 - p_2 ((PDD)) \quad (6b)$

M is the melt rate (mm d^{-1}), T_a is daily mean air temperature ($^{\circ}\text{C}$) and T_T is a threshold temperature fixed at 0°C . I_{pot} is the potential clear-sky incoming direct solar radiation (W m^{-2}), I_0 is the solar constant (1368 W m^{-2}), R_m and R are the mean and actual Sun-Earth distance, ϕ_a is the vertical clear-sky atmospheric transmissivity (0.75), P is the atmospheric pressure in Pa and P_0 is standard atmospheric pressure (101325 Pa). Z is the solar zenith angle, and θ is the incidence angle of the Sun on the surface. I is incoming shortwave radiation (W m^{-2}), and α is snow albedo, where PDD ($\text{mm }^{\circ}\text{C}^{-1} \text{ d}^{-1}$) is the positive degree-day sum since the last snowfall. The parameter p_1 represents a typical maximum albedo value for fresh snow (0.8) and p_2 is the empirical snow albedo decay parameter (0.21). RH is relative humidity.

Table 3 : Summary of model parameters values previously calibrated by Bouamri et al. (2018) and prescribed in this study.

Prescribed parameter	Description	Optimal Value	Unit	Calibrated parameter	Calibrated parameter	Description	Optimum value	Optimum value	Optimum value
DDF	Degree-day factor	2.7	$\text{mm d}^{-1} \text{ }^{\circ}\text{C}^{-1}$	TLP	Temperature lapse rate	Temperature lapse rate	Temperature lapse rate	0.56	$^{\circ}\text{C } 100 \text{ m}^{-1}$
MF	Melt factor	1.8	$\text{mm d}^{-1} \text{ }^{\circ}\text{C}^{-1}$	DPLR	Dew point lapse rate	Dew point lapse rate	Dew point lapse rate	-0.68	$^{\circ}\text{C } 100 \text{ m}^{-1}$
RF	Potential radiation factor	0.005	$\text{m}^2 \text{ mm W}^{-1} \text{ d}^{-1} \text{ }^{\circ}\text{C}^{-1}$	PLR	Precipitation lapse rate	Precipitation lapse rate	Precipitation lapse rate	0.35	km^{-1}
TF	Temperature factor	1.1	$\text{mm d}^{-1} \text{ }^{\circ}\text{C}^{-1}$	SWE_0	SWE-SCA threshold	SWE-SCA threshold	SWE-SCA threshold	4	mm
SRF_{in}	Global radiation factor	0.025	$\text{m}^2 \text{ mm W}^{-1} \text{ d}^{-1}$	Z_{max}	Maximum elevation difference	Maximum elevation difference	Maximum elevation difference	1000	m
TF	Temperature factor	0.6	$\text{mm d}^{-1} \text{ }^{\circ}\text{C}^{-1}$	T_{snow}	Temperature threshold for snow	Temperature threshold for snow	Temperature threshold for snow	2.5	$^{\circ}\text{C}$
SRF_{net}	Net short-wave radiation factor	0.07	$\text{m}^2 \text{ mm W}^{-1} \text{ d}^{-1}$	T_{rain}	Temperature threshold for rain	Temperature threshold for rain	Temperature threshold for rain	2.5	$^{\circ}\text{C}$
p_1	Fresh snow albedo	0.8	-						

Prescribed parameter	Description	Optimal Value	Unit	Calibrated parameter	Calibrated parameter	Description	Optimum value	Optimum value	Optimum value
p_2	Albedo decay parameter	0.21	-						
Subli	Constant sublimation rate	0.244	mm d ⁻¹						

Table 4 : Description of confusion matrix between simulated and MODIS SCA, and the evaluation metrics used for model assessment. TP: true positive, TN: true negative, FP: false positive, FN: false negative.

	SCA MODIS	SCA MODIS
SCA _{sim}	Snow	Snow free
Snow	TP	FP
Snow free	FN	TN
Metrics	Definitions	Definitions
TPR	$\frac{TP}{(TP+FN)}$	$\frac{TP}{(TP+FN)}$
TNR	$\frac{TN}{(TN+FP)}$	$\frac{TN}{(TN+FP)}$
FNR	$\frac{FN}{(FN+TP)}$	$\frac{FN}{(FN+TP)}$
FPR	$\frac{FP}{(FP+TN)}$	$\frac{FP}{(FP+TN)}$
HSS	$\frac{2 \times (TP \times TN - FP \times FN)}{(TP+FP) \times (FP+TN) + (TP+FN) \times (FN+TN)}$	$\frac{2 \times (TP \times TN - FP \times FN)}{(TP+FP) \times (FP+TN) + (TP+FN) \times (FN+TN)}$

Table 5 : Error statistics for calibration and validation of the precipitation lapse rate (PLR) at Rheraya catchment

Snowmelt models	Metrics	Calibration	Validation	Validation
	(km ⁻¹)	2003 to 2006	2007/2008	2009/2010
TI	BIAS	-3.45	-48.99	70.68
	NSE	0.85	-0.10	0.58
	RMSE	0.04	0.07	0.08
HTI	BIAS	1.27	-39.45	75.86
	NSE	0.85	0.19	0.54
	RMSE	0.04	0.06	0.08
ETIA	BIAS	15.38	-22.29	76.72
	NSE	0.78	0.60	0.53
	RMSE	0.05	0.04	0.08
ETIB	BIAS	10.66	-8.05	83.09
	NSE	0.83	0.78	0.47
	RMSE	0.05	0.03	0.09

Table 6 : HSS index and optimal SWE₀ and Z_{max} parameters obtained in calibration-validation

CALIBRATION	CALIBRATION	CALIBRATION
Models	TI	HTI

CALIBRATION	CALIBRATION	CALIBRATION
HSS	0.45	0.47
VALIDATION	VALIDATION	VALIDATION
	A- Optimal parameters sets of each model [SWE ₀ (mm), Z _{max} (m)]	A- Optimal parameters sets of each
	TI [3, 700]	HTI [4, 900]
HSS	0.46	0.47
	B- Mean optimal parameter [SWE ₀ = 4 mm, Z _{max} = 1000 m]	B- Mean optimal parameter [SWE ₀ = 4 mm, Z _{max} = 1000 m]
HSS	0.45	0.47

Figures captions

Graphical Abstract

Figure 1. Geographical location of the Rheraya basin and weather stations

Figure 2. Available observations during the study period (2003-2016) for the different weather stations in the Rheraya catchment. RH: relative humidity; Ta: air temperature; Pr: total precipitation.

Figure 3 : Flowchart describing the steps for processing MODIS data and comparing MODIS and simulated snow cover area (SCA). Purple color: data source, pink: sub-result, and gray: main results.

Figure 4. Partition of precipitation into snowfall and rainfall. (a) Simulated vs. observed precipitation after calibration of the fixed rain-snow partition temperature thresholds. (b) Observed frequencies of snow, rain, and mixed precipitation events per one-degree temperature bin at CAF weather station over the 2003-2016 period.

Figure 5. Calibration and validation of precipitation lapse rate (PLR) on observed SWE at AWS Oukaimeden-SM. (a-c) calibrated years, respectively 2003-2004, 2004-2005, 2005-2006; (d-e) validated years, respectively, 2007-2008 and 2009-2010.

Figure 6 . Sensitivity of model SCA simulation performance to Z_{max} and SWE₀ parameters. The model performance is assessed with the mean HSS index over the calibrated period. Optimal parameter values are indicated by asterisks (*). (a) TI; (b) HTI; (c) ETIA; (d) ETIB.

Figure 7. Time series of (a) simulated mean snow water equivalent (SWE), and (b) simulated mean SCA (fractional snow cover area: fSCA) of all models vs MODIS and (c) errors statistics over the entire period 2003-2016 in the Rheraya catchment.

Figure 8 : Seasonal cycle of mean simulated snow water equivalent (SWE) (a) over snow-covered area only; (b) over the whole basin; (c) mean simulated fSCA vs MODIS; (d-e) difference between radiative models and reference TI model for a-b panels; (f) difference between modelled and MODIS fSCA.

Figure 9. Seasonal cycle of HSS index over (a) calibration; (b) validation; (c) entire period. Lower row: corresponding differences between enhanced radiative models and classical temperature index (TI) model.

Figure 10. (a) Distribution of mean SCA per elevation range, and hypsometric curve at 100 m. (b) Median of HSS index of all models per elevation, (c, d, and e) HSS differences between radiative and classical model per elevation range over Rheraya basin.

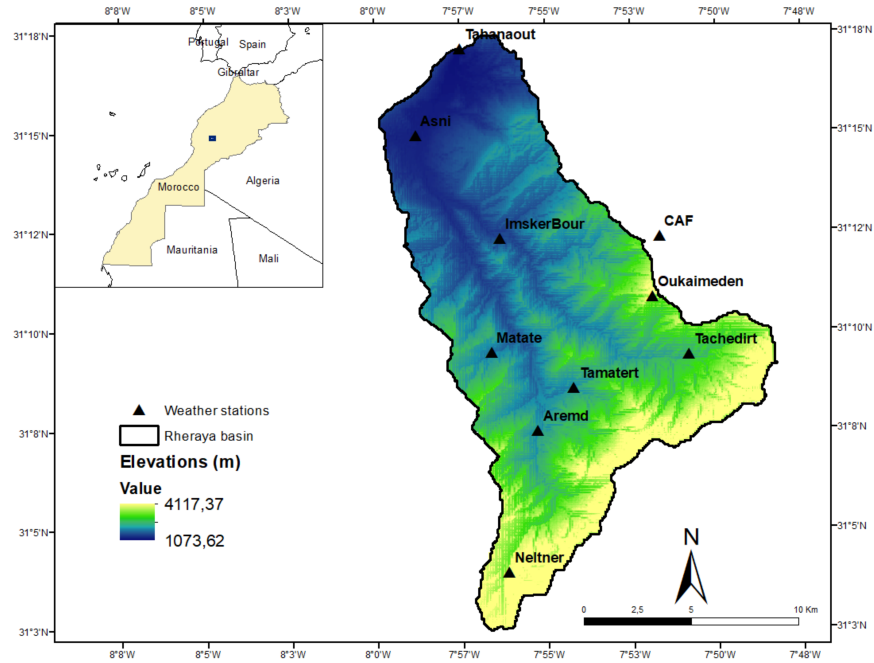
Figure 11. SCA classification errors per elevation range in the Rheraya watershed; 1st row: true positive rate (TPR); 2nd row: true negative rate (TNR); 3rd row: false positive rate (FPR); 4th row: false negative rate. (a) Median error rate; (b, c, and d) differences between radiative and classical TI model.

Figure 12. Annual average simulated snow cover duration (SCD) vs MODIS SCD during calibration (light blue) and validation (dark blue), with statistic errors for all model (a) TI; (b) HTI; (c) ETIA; (d) ETIB.

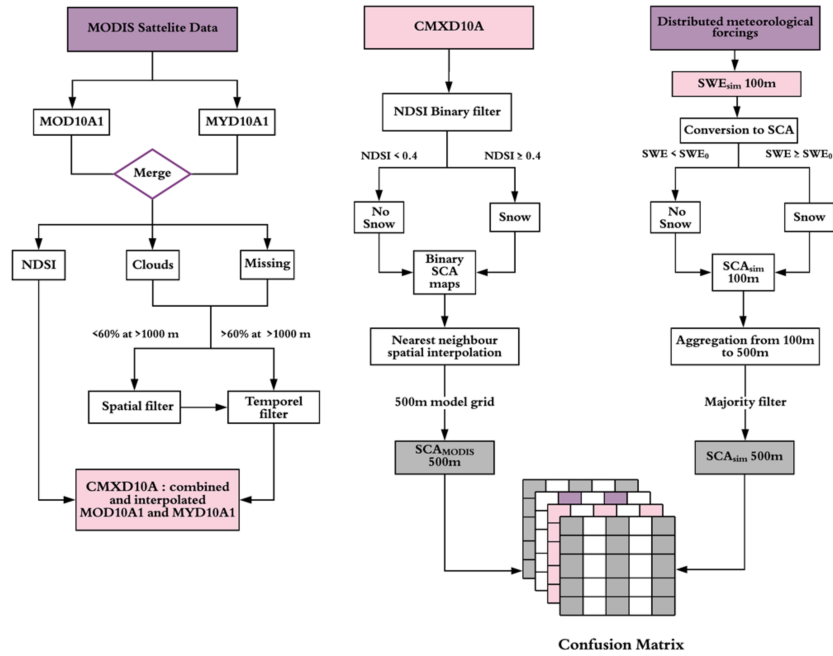
Figure 13. SWE and melt per elevation band in the Rheraya catchment. (a) Median SWE for all models; (b-d) SWE differences between radiative and classical TI model; (e) median melt rate for all models; (f-h) melt differences between radiative and TI model

Figure 14. Snow cover duration (SCD) per elevation band in the Rheraya catchment. (a) Median SCD and DEM median northern exposure index at 100 m resolution; (b, c, and d) SCD differences between radiative and classical model at 100 m. (e-h): same as (a-b) but SCD is aggregated from 100 m to 500 m and the northern exposure index (‘NS index’) is calculated on a DEM aggregated from 100 m to 500 m. (i-l) Differences between each model 500 m SCA and MODIS.

Figure 15. Mean SWE, melt rate, and snow cover duration (SCD) by aspect. (a) Mean SWE (mm); (b) melt rate (mm d⁻¹); (c) SCD (days) at 100 m resolution; (d) SCD (days) at 500 m resolution and (e) DEM aspect at 100 and 500 m resolution.

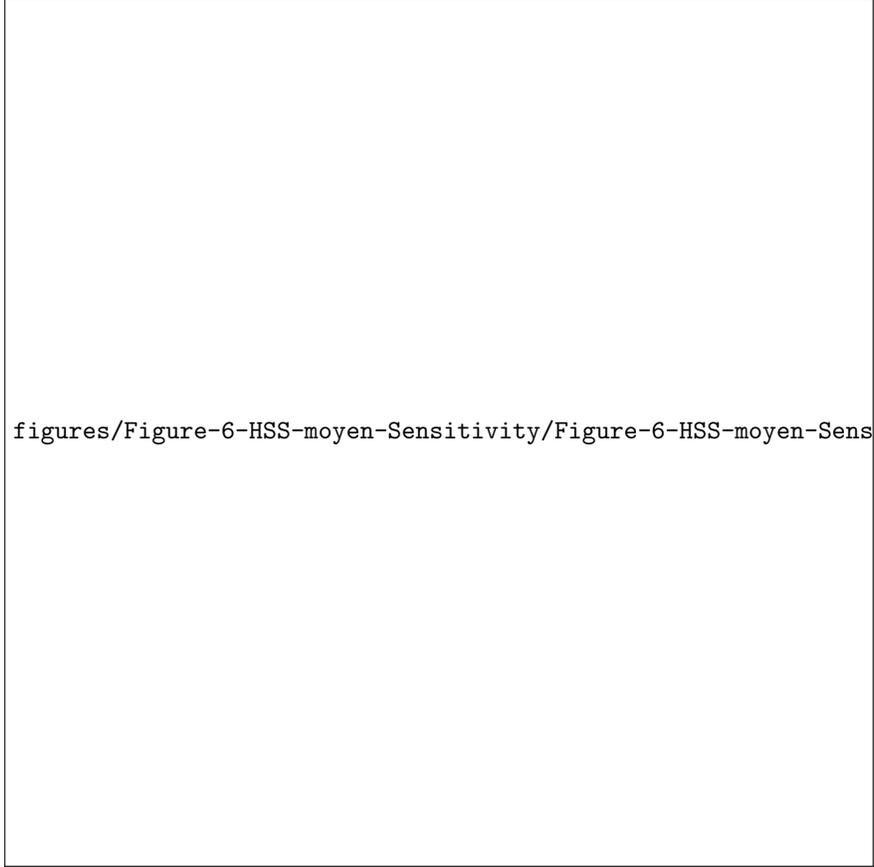


figures/Figure-2-Avalibility-Param-All-station/Figure-2-Avalibility-Param-All-station-eps



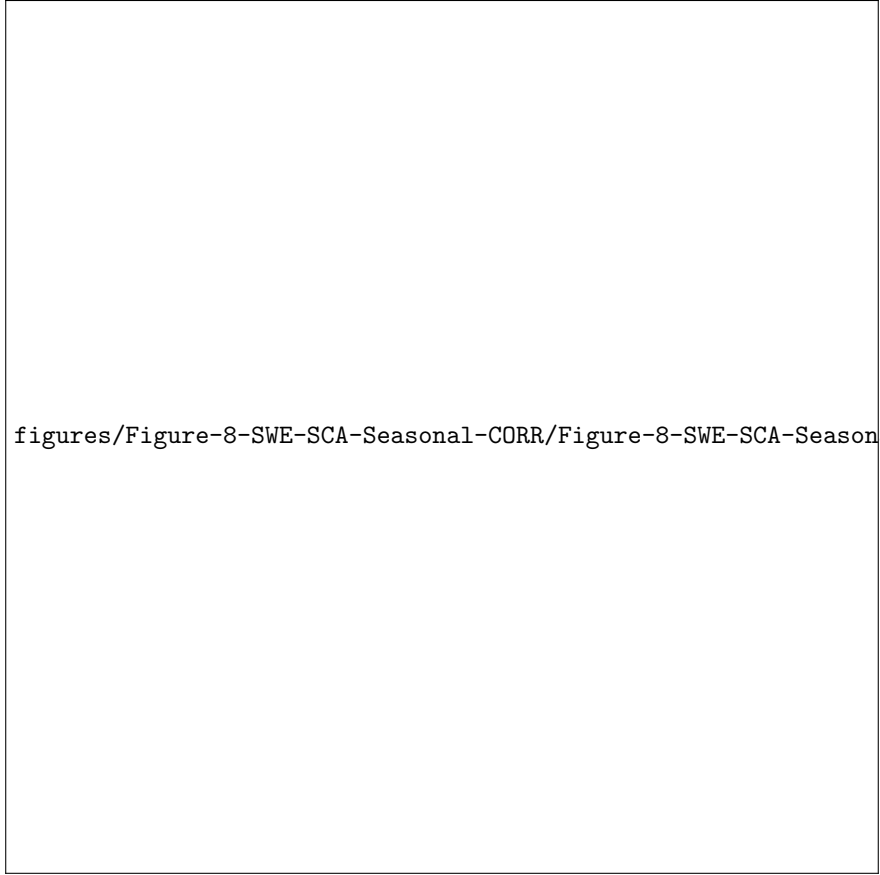
figures/Figure-4-RainSnow-discr/Figure-4-RainSnow-discr-eps-converted-to.pdf

figures/Figure-5-CalVal-Pgd-DiffSWE/Figure-5-CalVal-Pgd-DiffSWE-eps-converted-to.pdf



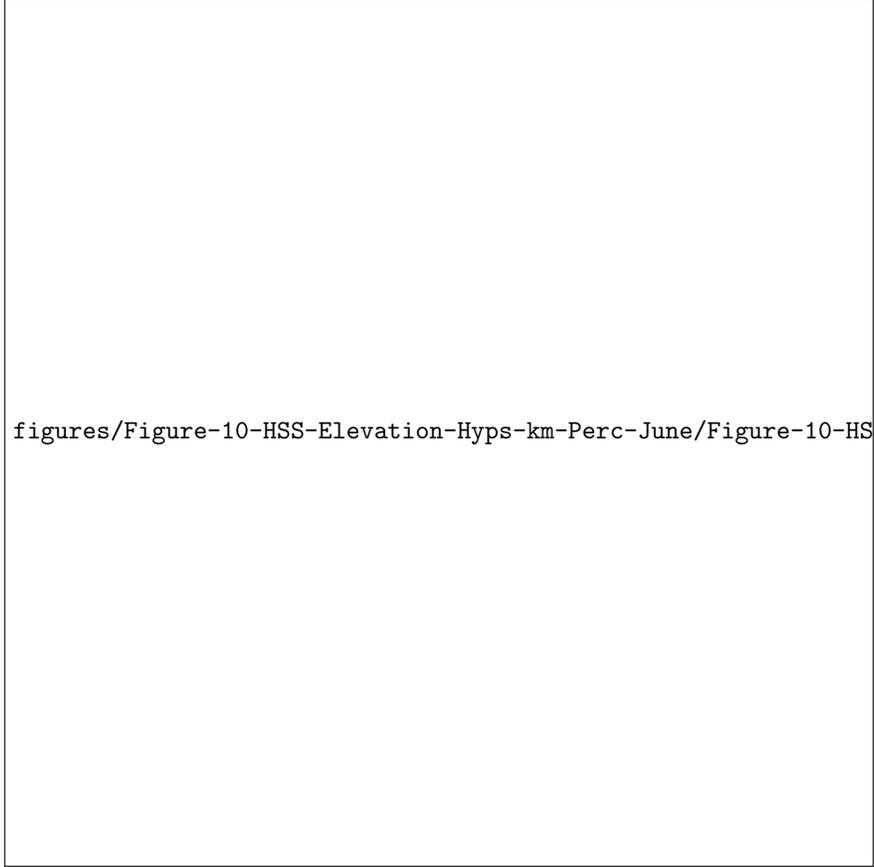
figures/Figure-6-HSS-moyen-Sensitivity/Figure-6-HSS-moyen-Sensitivity-eps-converted-to.pdf

figures/Figure-7-TS-SWEsim-SCAsim-ALL-Period-LA/Figure-7-TS-SWEsim-SCAsim-ALL-Period-LA-e

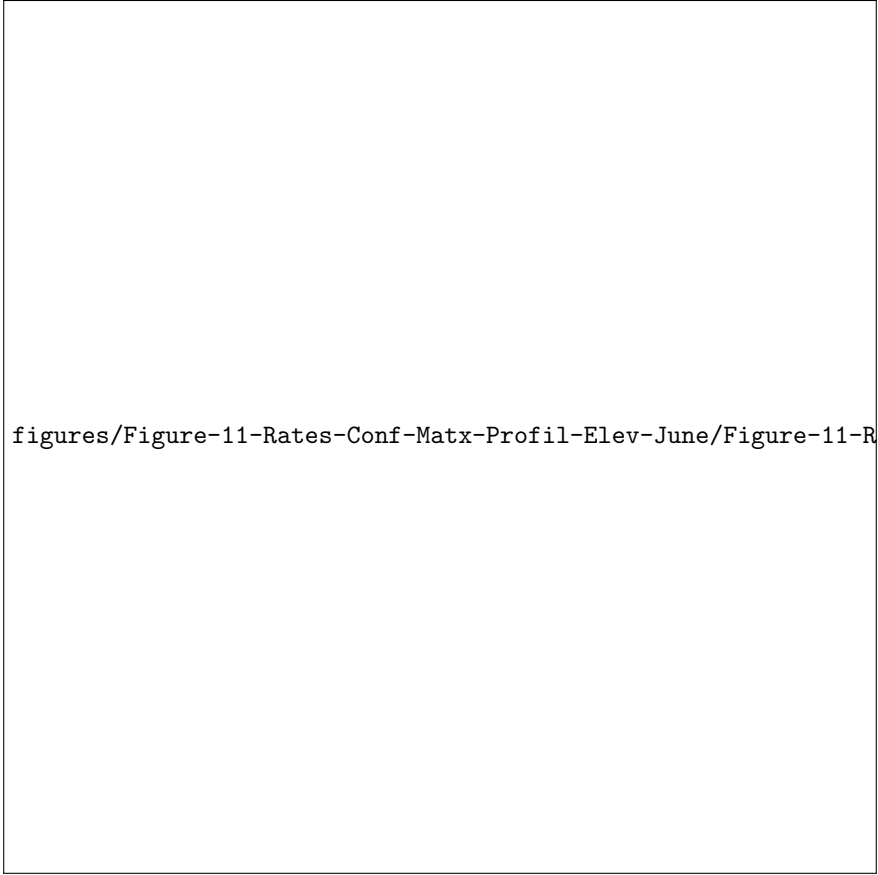


figures/Figure-8-SWE-SCA-Seasonal-CORR/Figure-8-SWE-SCA-Seasonal-CORR-eps-converted-to.pdf

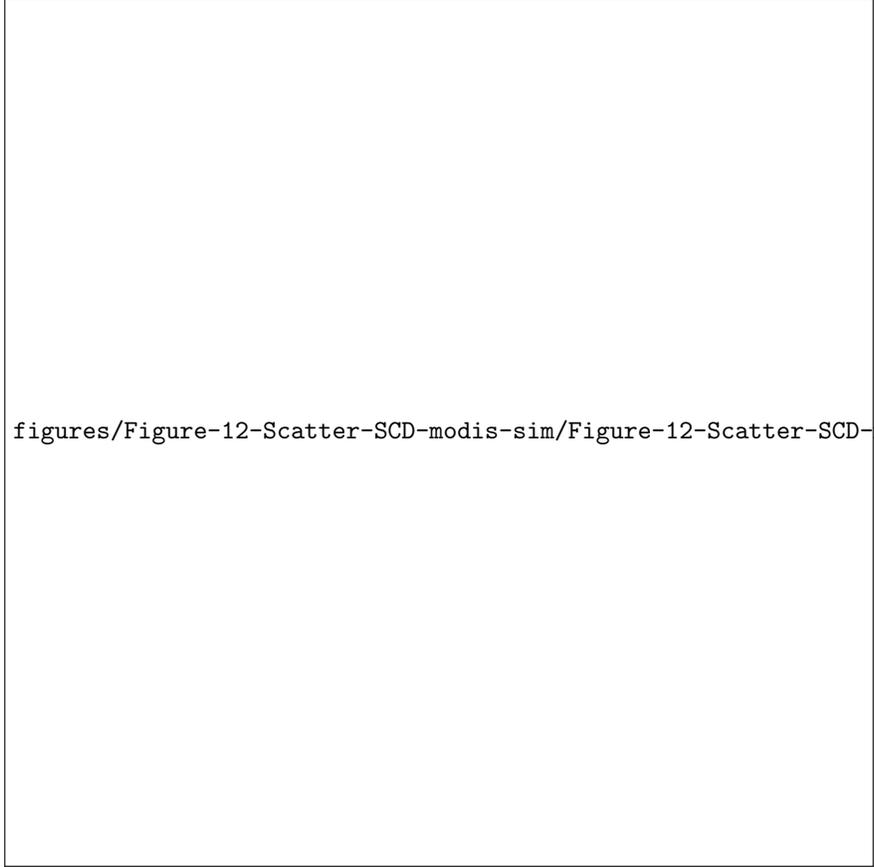
figures/Figure-9-Seasonal-HSS-All-June/Figure-9-Seasonal-HSS-All-June-eps-converted-to.pdf



figures/Figure-10-HSS-Elevation-Hyps-km-Perc-June/Figure-10-HSS-Elevation-Hyps-km-Perc-Ju



figures/Figure-11-Rates-Conf-Matx-Profil-Elev-June/Figure-11-Rates-Conf-Matx-Profil-Elev-



figures/Figure-13-SWE-Melt-Elev/Figure-13-SWE-Melt-Elev-eps-converted-to.pdf

figures/Figure-14-SCD-Elevation-CORR-June/Figure-14-SCD-Elevation-CORR-June-eps-converted

figures/Figure-15-Aspect-vsSWE-SCD-melt/Figure-15-Aspect-vsSWE-SCD-melt-eps-converted-to.